Episodic subduction patches in the western North Pacific identified from BGC-Argo float Data

Shuangling Chen[1], Mark L. Wells[2,1], Rui Xin Huang[3], Huijie Xue[4,5], Jingyuan Xi[1], Fei Chai[1,6*]

[1] State Key Laboratory of Satellite Ocean Environment Dynamics, Second Institute of Oceanography, Ministry of Natural Resources, Hangzhou, China

[2] School of Marine Sciences, University of Maine, Orono, ME, USA

[3] Woods Hole Oceanographic Institution, Woods Hole, MA, USA

[4] State Key Laboratory of Marine Environmental Science, Xiamen University, Xiamen, China

[5] College of Ocean and Earth Sciences, Xiamen University, Xiamen, China

[6] School of Oceanography, Shanghai Jiao Tong University, Shanghai, China

[*]Corresponding author: Fei Chai (fchai@sio.org.cn)

Abstract

Subduction associated with mesoscale eddies is an important but difficult to observe process that can efficiently export carbon and oxygen to the mesopelagic zone (100-1000db). Using a novel BGC-Argo dataset covering the western North Pacific (20-50°N, 120-180°E), we identified imprints of episodic subduction using anomalies in dissolved oxygen and spicity, a water mass marker. These subduction patches were present in 4.0% (288) of the total profiles (7,120) between 2008 and 2019, situated mainly in the Kuroshio Extension region between March and August (70.6%). Roughly 31% and 42% of the subduction patches were identified below the annual permanent pycnocline depth (300m *vs.* 450 m) in the subpolar and subtropical regions, respectively. Around half (52%) of these episodic events injected oxygen-enriched waters below the maximum annual permanent thermocline depth (450 db), with >20% occurring deeper than 600 db. Subduction patches were detected during winter and spring when mixed layers are deep. Oxygen inventory within these subductions is estimated to be on the order of 64 to 152 g O_2 m^{-2}. These mesoscale events would markedly increase oxygen ventilation as well as carbon removal in the region, both helping to support the nutritional and metabolic demands of mesopelagic organisms. Climate-driven patterns of increasing eddy kinetic energies in this region imply that the magnitude of these processes will grow in the future, meaning that these unexpectedly effective small-scale subduction processes need to be better constrained in global climate and biogeochemical models.

Keywords: dissolved oxygen; spicity; BGC-Argo; subduction; North Pacific

1. Introduction

Ocean subduction is the process of transporting water from the wind-mixed surface layer into or below the permanent thermocline, resulting in the efficient injection of heat, carbon and oxygen to the ocean interior (Fig. 1). Subduction therefore plays an important role in regulating global climate and carbon cycles (Sabine et al., 2004; Qu & Chen, 2009; Stukel et al., 2017 & 2018; Boyd et al., 2019; Martin et al., 2020). Many studies focus on the subduction of mode waters driven by large-scale circulation, and the seasonal cycle of the mixed layer dynamics (Williams, 2001; Qu et al., 2002; Qiu et al., 2007; Koch-Larrouy et al., 2010; Kawakami et al., 2015; Nie et al., 2016). But recent advances have highlighted the importance of small-scale (1-100 km) dynamical processes on vertical transport and biogeochemistry in the upper ocean, driven by mesoscale eddies and sub-mesoscale processes (Lévy et al., 2001; Xu et al., 2014; Omand et al., 2015; McGillicuddy, 2016; Llort et al., 2018; Resplandy et al., 2019). Ocean general circulation models typically resolve the large-scale subduction of mode waters (Koch-Larrouy et al., 2010) but cannot accurately capture small-scale, short-term subduction processes because of their episodic characteristics (Xu et al., 2014; Llort et al., 2018).
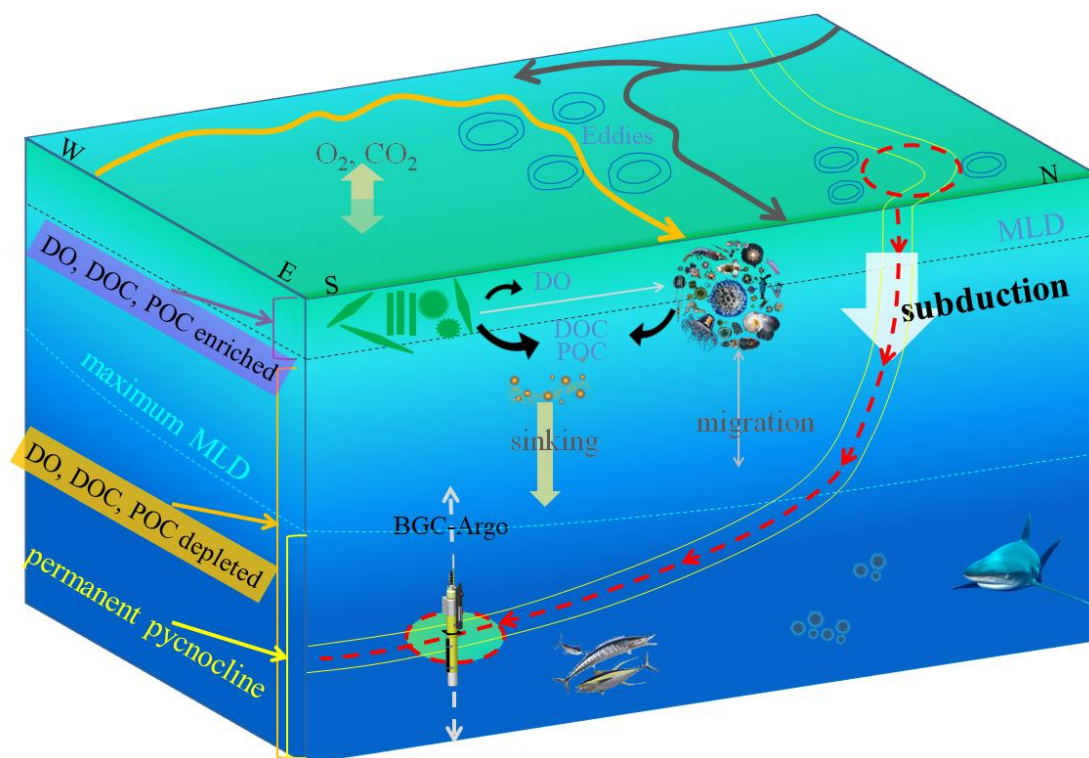
Fig. 1 An illustration of the Kuroshio and Oyashio extension region depicting the different modes of carbon export below the maximum annual mixed layer depth; the biologcial gravitational pump (sinking export, zooplankton migration) and subduction in the region of the Kuroshio and its extension (yellow line) and Oyashio and its extension (grey line). The subducted surface waters, apparently driven by mesoscale eddy processes, travel along isopycnal surfaces transporting water containing high dissolved oxygen (DO), dissolved organic carbon (DOC) and slowly sinking particulate organic carbon (POC) into the mesopelagic zone (low DO, DOC,

and POC). The green layer represents the euphotic zone, and the blue layer below is the mesopelagic zone.

Subduction associated with mesoscale and sub-mesoscale dynamics has been observed at higher latitudes in the North Atlantic (Omand et al., 2015) and Southern Oceans (Llort et al., 2018), and similar processes are shown to occur in Kuroshio Extension (KE) region in the western subtropical Pacific. Shipboard sampling techniques have been used there to identify small water parcels within the main thermocline having low potential vorticity, elevated dissolved oxygen (DO), and anomalous salinity; signals indicative of small-scale subduction (Yasuda et al., 1996; Okuda et al., 2001; Oka et al., 2009). Analogous phenomena have been observed in mooring data from the region (Nagano et al., 2016; Inoue et al., 2016a; Kouketsu et al., 2016; Zhu et al., 2021), and more focused sampling of anticyclonic eddies with Argo floats (Zhang et al., 2015; Inoue et al., 2016b) and SeaGliders (Hosoda et al., 2021) confirm the existence of discrete subsurface water mass exchanges. These episodic features will contribute to both ventilation of the mesopelagic zone as well as export of dissolved inorganic and organic carbon from surface waters (i.e., the solubility pump (Sarmiento & Gruber, 2006), but their frequency, spatial extent and lifetimes remain unknown (Hosoda et al., 2021).

Eddy-associated processes that generate vertical transport of productive and detrital planktonic biomass into the mesopelagic zone affect not only carbon export but also carbon sequestration time scales (i.e., time that carbon remains within the ocean interior). In general, sequestration time scales are proportional to the depth of injection but the more important factor is whether these injections extend below the annual maximum mixed layer depth (MLD), or permanent pycnocline, which hinders its return to the atmosphere (Boyd et al., 2019). Although eddy-subduction has the potential to contribute significantly to global carbon export, evidence of the subsurface fate of injected carbon has been indirect and patchy (Estapa et al., 2019), highlighting the challenge of detecting and quantifying carbon export associated with mesoscale and sub-mesoscale processes.

The uncertainty about the contribution of eddy subduction to carbon and oxygen transport into the mesopelagic and deeper ocean interior has ramifications for both biogeochemical and ecological processes (Fig. 1). The transport of freshly produced particulate and dissolved organic carbon, along with oxygen, from surface waters to the mesopelagic zone is critical for balancing upper ocean carbon budgets (Emerson, 2014) and supporting the nutritional demands of mesopelagic organisms (Dall'Olmo et al., 2016). The knowledge gap in these episodic processes is particularly evident in the mid-latitude western North Pacific, where mesoscale eddies, recirculation gyres, fronts, and jets are amplified under the influence of the Kuroshio and Oyashio currents and their extensions (Nishikawa et al., 2010). Shoaling of the maximum annual MLD in this region relative to higher latitudes (Cronin et al., 2013; Palevsky & Doney, 2018) has the potential to increase carbon sequestration efficiency and oxygenation of the deep mesopelagic zone (Bushinsky & Emerson, 2018).

105 Here we investigate small-scale subduction events in the western North Pacific
106 region over the past decade (2008-2019). These events were identified with a new
107 algorithm utilizing anomalies of apparent oxygen utilization (AOU; a proxy for
108 dissolved and particulate organic matter degradation) and potential spicity (π; a
109 characteristic water mass marker) obtained from multiple biogeochemical Argo
110 (BGC-Argo) datasets (Claustre et al., 2020; Chai et al., 2020). These findings show
111 the spatial and temporal distributions of subduction patches reflecting episodic
112 injection processes that contribute to the missing fraction of carbon and oxygen
113 export into the deep twilight zone (Emerson, 2014; Martin et al., 2020), but also
114 have the potential to become increasingly significant under future climate scenarios.

115 **2. Data and Methods**

116 **2.1 Data**

117 After the standard data quality control, 7,120 profiles from 43 BGC-Argo floats in
118 the western North Pacific (20-50°N, 120-180°E) between 2008 and 2019 were
119 selected (Fig. 2). All of these profiles contained measurements of temperature,
120 salinity, pressure, and dissolved oxygen (DO, μmol/kg). The upper 1000db of the
121 ocean was sampled in each profile and the typical profiling interval was between 5-
122 10 days, with the floats parking at 1000db depth in between. The typical vertical
123 sampling frequency was every 5db, 10db, and 50db for depth intervals of 0-100db,
124 100-500db, and 500-1000db, respectively. Some floats were set with daily profiling
125 and higher vertical frequency (e.g., every 2db) for specific purposes.
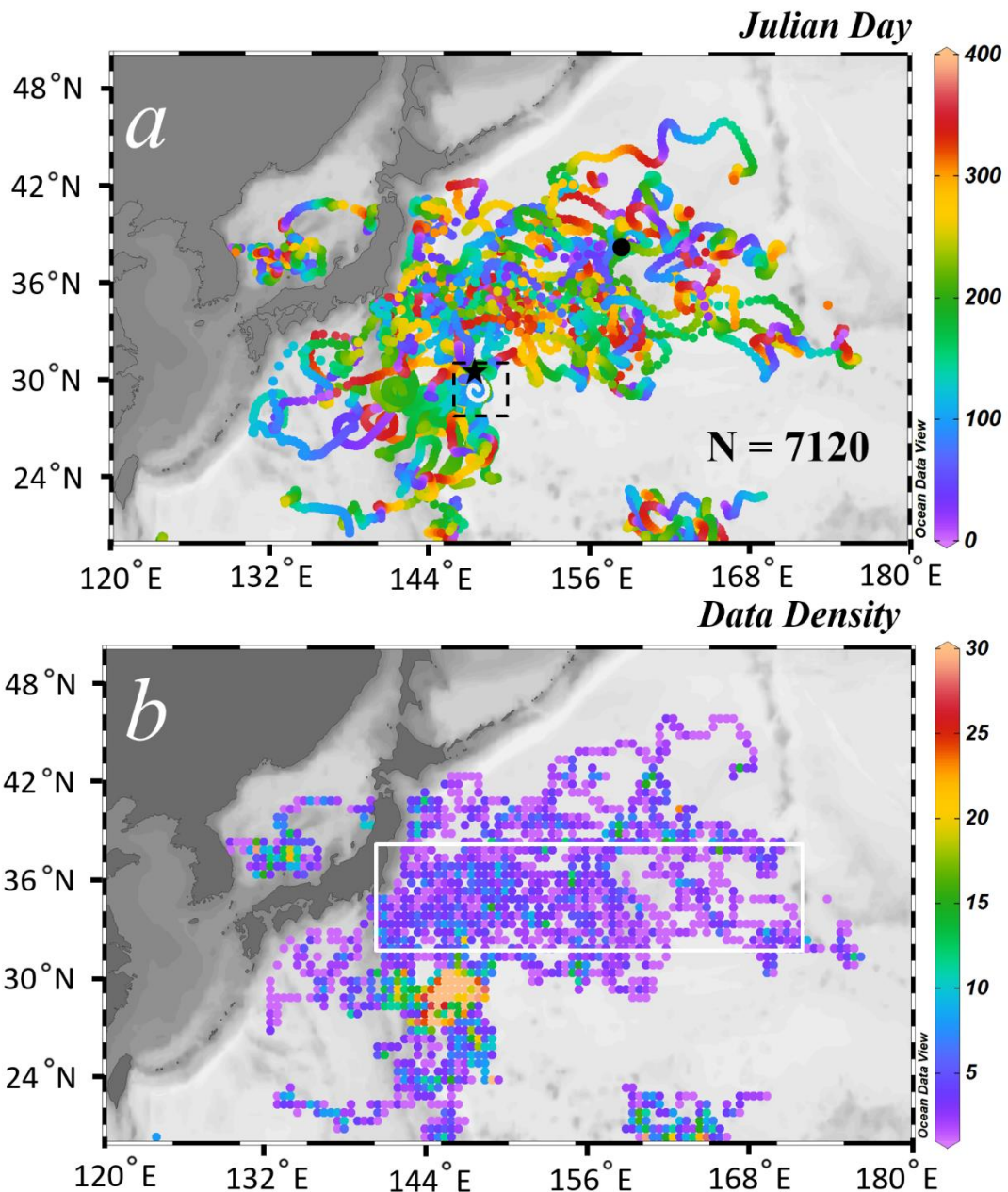
Fig. 2 Horizontal distribution of the QCed BGC-Argo data profiles between 2008 and 2019 in the western North Pacific. The Argo profiling tracks are color coded by Julian day (a) and data density (number of available profiles) for each grid ($0.5^{\circ} \times 0.5^{\circ}$) (b). The location of Station No. 234 from float MD5904034 is denoted by the black dot in (a) (see Fig. 3); the white curve inside the dashed box represents the trajectory of float MR2901556 between July 28th and August 18th in 2014, and the black star indicates the beginning of the float trajectory during this period (see Fig. 4). The white box in (b) denotes the region with strong energetic ocean processes (i.e., Kuroshio-Oyashio Extension, popular with eddy activities).

136   All BGC-Argo variables were vertically smoothed with a 3-bin running average to
137   remove sharp noises or spikes (Llort et al., 2018). Two key variables, apparent
138   oxygen utilization (AOU) and potential spicity (π), were derived from the direct
139   measurements. Specifically, AOU is defined as the difference between saturated
140   oxygen concentration (O_{sat}) and DO, and O_{sat} is estimated from temperature and
141   salinity (Garcia & Gordon, 1992). AOU is a proxy for water mass age which reflects
142   the microbial respiration of dissolved and particulate organic matter (Sarmiento &
143   Gruber, 2006). Potential spicity referenced to the surface pressure is calculated from
144   pressure, temperature and salinity following Huang et al. (2018). Sea water is a two-
145   component system. Water mass anomaly is commonly analyzed in terms of
146   (potential) temperature and salinity anomaly, and isopycnal analysis is also widely
147   used. By definition, temperature and salinity anomaly on an isopycnal surface is
148   density compensated; thus, water mass anomaly on an isopycnal surface is
149   commonly described in term of another thermodynamic variable, which is called
150   spice, spiciness or spicity. Over the past decades, there have been different
151   definitions of such a thermodynamic variable; however, a most desirable property of
152   such a thermodynamic function is that it is orthogonal to the density. Recently,
153   Huang et al. (2018) proposed a potential spicity function (π) by the least square
154   method, which is practically orthogonal to the potential density, with the root-mean-
155   square of angle deviation from orthogonality at the value of $0.0001°$. Therefore,
156   combining density and spicity gives rise to an orthogonal coordinate system. It is the
157   thermodynamic variable we used in this study, which allows differentiating water
158   masses with distinct thermohaline properties but similar density. In addition,
159   potential density (σ) referenced to the surface pressure was derived from pressure,
160   temperature and salinity based on the thermodynamic equation (TEOS-10
161   (McDougall & Barker, 2011)); and MLD was estimated based on a threshold (0.05
162   kg/m^3) of the difference in density from a near-surface value (i.e., at 10db) (Brainerd
163   & Gregg, 1995). All these derived variables were calculated for each of the 7,120
164   profiles.

165   In addition to the BGC-Argo float data, satellite data of daily sea level anomalies
166   (SLA) and daily geostrophic velocity anomalies (*u'* and *v'*) between 1993 and 2018
167   were also processed. The geostrophic velocity anomalies were used to calculate the

168   eddy kinetic energy (EKE) as $EKE = \frac{1}{2}\sqrt{u'^2 + v'^2}$. These data were used to identify

169   the spatial relationship between surface mesoscale circulation and the float profiles.

170   **2.2 Methods**

171   2.2.1 subduction detection

172   When a BGC-Argo float passes through a parcel of water injected from the mixed
173   layer, it captures coherent anomalous features in AOU and π distinct from the
174   surrounding waters (Fig. 1). These anomalies can be used to identify subduction
175   patches that are indicators of subduction events occurring in the vicinity (Omand et
176   al., 2015; Llort et al., 2018). Quantifying anomalies in AOU and π (denoted as Δ_{AOU}

and Δ_π) requires defining the reference values of AOU and π at the mean state of the profile without subduction. Llort et al. (2018) used the 20-bin running averages of the profiles as the references, however, we found that this approach could dampen the subduction signal and thus miss subduction patches as well as misidentify other signals as subduction (see Fig. S1). To avoid misreporting these anomalies, a revised detection method was developed by trial and error, as shown in example profiles of AOU, π, DO and σ for Station No. 234 of float MD5904034 (Fig. 3; see Fig. 2a for its sampling location). Two subduction patches are visually apparent at ~230db and ~300db (yellow shades in Fig. 3a & 3b). The identification of the lower subduction patch at ~300db from the spicity profile is briefly described below and is illustrated in Fig. 3c:

1. Calculate the slopes (i.e., first-order derivative) for profiles of AOU and π against depth;

2. Locate the peaks in AOU and π profiles (e.g., the blue star in Fig. 3c) based on their slopes. Specifically, if at one sampling point the slope changes from positive to negative when moving downwards, it is called a negative peak and vice versa. Only the negative/positive peaks in π associated with a negative peak in AOU are considered, as only negative AOU anomalies indicate potential water transport from the surface mixed layer (Llort et al., 2018);

3. Locate the coherent peaks in both AOU and π, and mark their depths as the targeted locations (represented by pressure, p) for potential subduction patches;

4. Calculate the peak Δ_π at each targeted pressure. For the case of a negative (positive) peak, identify the maximum (minimum) values of π within the depth ranges of $[p-\Delta p, p]$ and $[p, p+\Delta p]$, respectively (green triangles in Fig. 3c), and the depth interval $\Delta p=100$db is chosen, considering the general vertical scale (i.e., a few tens of meters) of the eddy-induced subduction features (Zhang et al., 2015; Hosoda et al., 2021); the reference profile is defined by the straight line in between. The anomaly Δ_π (red bracket in Fig. 3c) is defined as the difference between the reference profile and the original profile of π at pressure p (green star in Fig. 3c);

5. Calculate Δ_{AOU} using the same method, independent of Δ_π;

6. The thresholds used to determine whether the signals meet the criteria of a subduction patch or not were set to -10 μmol/kg for Δ_{AOU} and ±0.05 kg/m^3 for Δ_π following Llort et al. (2018).

213
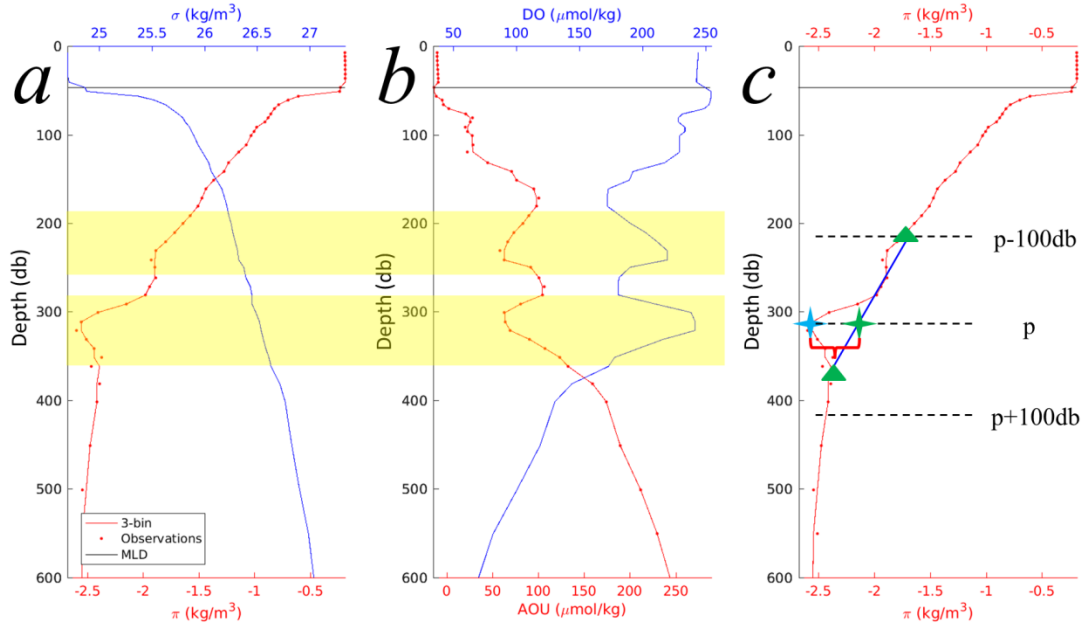
Fig. 3 Vertical property distributions of profile No. 234 (on June 24th 2016) of float MD5904034 (the black dot in Fig. 2a) demonstrate subduction patches observed by the BGC-Argo floats. (a) The profiles of potential density (σ, blue line) and potential spicity (π, red dotted line), (b) the profiles of DO (blue line) and AOU (red dotted line), and (c) same spicity profile as in (a), which is used to demenstrate the steps to detect subduction signals described in Methods. Note that the red dots in each panel represent the raw field observations, the overlaid red curves are the 3-bin running averages to remove sharp noises or spikes, and they are used to calculate the anomalies in AOU and π, and the black line represents the MLD. The yellow shades in (a) and (b) highlight the subduction features identified using the detection method in (c).

The refined algorithm presented here had improved performance for detecting subduction patches in these BGC-Argo profile data than that used in previous studies (Llort et al., 2018) (see Fig. S1). The main difference in our approach is in selecting the frame of reference for identifying AOU and π anomalies from irregular features in "typical" vertical profiles.

The sensitivity of the method to the interval of Δp (in step 4) was investigated by varying Δp between 70db and 130db (see Table S1). For Δp of 100±3db (i.e., 97db, 98db, 99db, 101db, 102db, and 103db), less than 7 ($\leq 2\%$) subduction patches were missed, and the resulted Δ_{AOU} and Δ_{π} show a RMSD of $\leq 3.8\mu$mol/kg ($\leq 8.3\%$) and ≤ 0.03 kg/m3 ($\leq 9.2\%$). More details are provided in Text S1. The sensitivity analysis suggests the validity and robustness in the choice of Δp of 100db. After verifying that our approach better captured subduction indicators in a subset of BGC-Argo data from this region, the algorithm was applied to all profiles to identify the locations, depths, time and strengths (i.e., Δ_{AOU}, Δ_{DO} and Δ_{π}) of the subduction patches.

240   2.2.2 Quantification of oxygen export

241   For all the subduction patches identified using the method developed above, we
242   obtain a first order estimate of oxygen export based on the DO anomalies (ΔDO)
243   with the assumptions that: 1) the surface processes initiating these subduction events
244   generated similar levels of DO (i.e., surface phytoplankton production), and 2) the
245   water parcels containing this DO are subducted into the ocean's interior.

246   We estimated the average oxygen inventories within the water column based on the
247   BGC-Argo profiles. We calculated DO inventories (per m^2) through these features in
248   two ways: integration of the anomaly above the estimated baseline (Eq. 1) and by
249   using the anomaly peak height (Eq. 2) (see Fig. 3c)..

250   The equation for the integrated estimates for each profile is:

251   Oxygen Inventory$_{IA}$ (g O$_2$/m^2) $= \sum_{z=p1}^{z=p2} \Delta DO_Z$ (Eq. 1)

252   where ΔDO_z is the DO anomaly at depth z within the water column of the
253   subduction patch, and the integrated areas (IA) of DO anomalies are converted from
254   μmol kg^{-1} to mg m^{-2} based on seawater density.

255   The inventory calculated using peak height (PH) approach is:

256   Oxygen Inventory$_{PH}$ (g O$_2$/m^2) $= \Delta_{DO\_peak} \times H$ (Eq. 2)

257   where H is the thickness (i.e., vertical height between the green triangles in Fig. 3c,
258   in unit of m) of the subduction patch and the Δ_{DO_peak} is the maximum anomalous
259   value of DO converted to mg m^{-2} as above. The oxygen inventory using the peak
260   height method represents the maximum potential of anomalous DO inventory within
261   the subduction patch.

262   **3. Results and Discussion**

263   **3.1 Case study: Detecting subduction in BGC-Argo datasets**

264   Subduction associated with eddy pumping is a recognized important contributor to
265   the transfer of carbon and other materials from the surface euphotic layer to the
266   ocean interior (McGillicuddy, 2016; Bord et al., 2019), but investigating the spatial
267   distributions, physical dynamics, and biogeochemical consequences of these
268   episodic small-scale processes is difficult. The BGC-Argo program provides an
269   exceptional data resource for this purpose (Claustre et al., 2020; Chai et al., 2020),
270   but detecting subduction signals where differences among water masses are small is
271   challenging.

272   Subduction patches below the seasonal and permanent pycnoclines can be identified
273   in vertical profiles by anomaly matrices of temperature, salinity, and dissolved
274   oxygen (DO). Examples of these events are illustrated in time-series from the BGC-
275   Argo profiling float (MR2901556), between July 28th and Aug. 18th 2014 (Fig. 4).

Positioned on the southern perimeter of the Kuroshio Extension region, the surrounding ocean conditions are less energetic, with less eddy activities and small sea level anomalies. During the observation period, the float was trapped in a warm-core eddy (Fig. S2), and moved from the margin of the eddy to the eddy core, as indicated by the graduate increase of depth of the anomalous patch (right panels of Fig. 4). Due to the vertical cruising of the Argo profiler in an environment with velocity shear, it may sample different parts of the same subduction patch, as indicated by slightly different depths, and anomalous spicity and oxygens concentration. Here, intermittent patches of elevated spicity (π), lower AOU, and greater dissolved oxygen are visible in the upper 600 db (Boxes 1-3, Fig. 4). Potential spicity (π), a parameter dependent on pressure, temperature and salinity (Huang et al., 2018), is a sensitive indicator of water mass differences. AOU is the difference between the measured dissolved oxygen concentration and its equilibrium saturation concentration in water with the same physical and chemical properties. It reflects the degree of progressive microbial decomposition of organic matter since the water was last at the surface in contact with the atmosphere (Garcia & Gordon, 1992; Sarmiento & Gruber, 2006). Despite this oxygen consumption, these injected waters retain excess net oxygen concentrations relative to the surrounding mesopelagic zone (Fig. 4d).
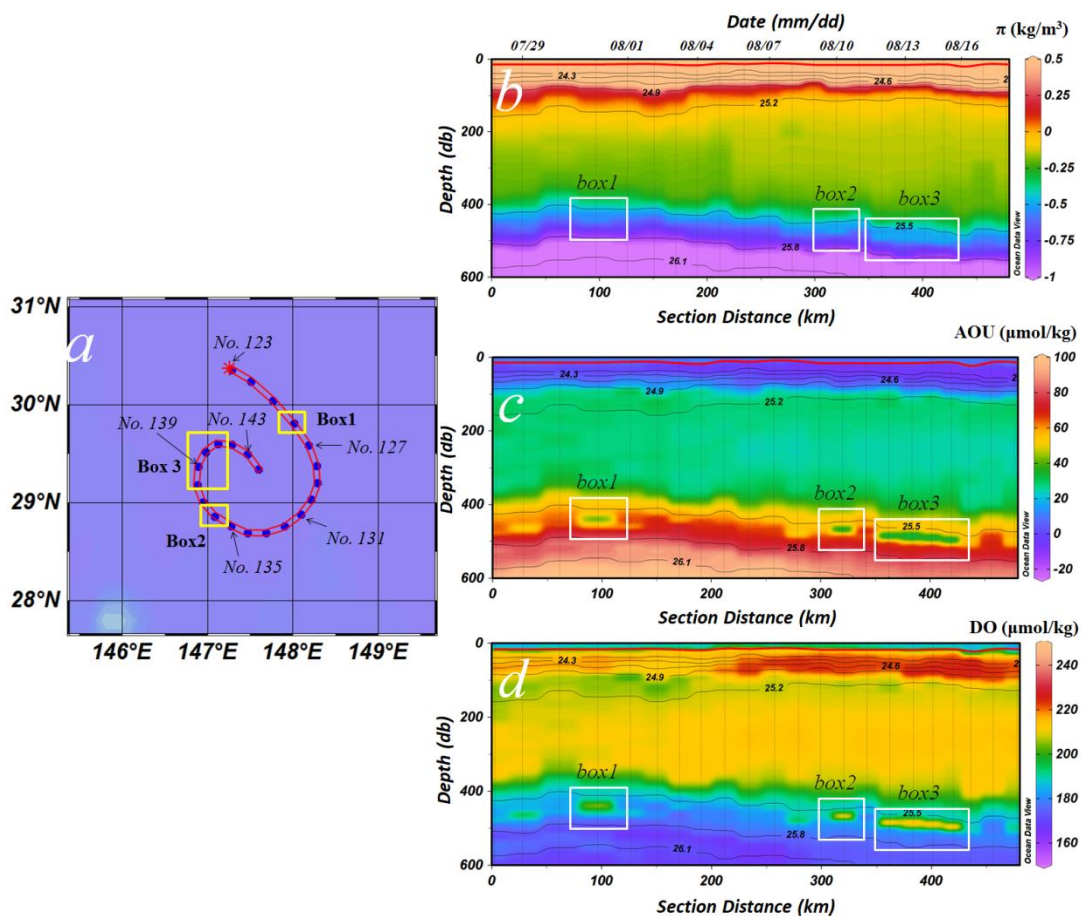
Fig. 4 Trajectory of float MR2901556 between July 28th 2014 (Station No. 123) and August 18th, 2014 (Station No. 144) (a) and its time series of π (b) AOU (c) and DO (d). Vertical lines in (b), (c) and (d) represent the Bio-Argo profiles, and the section distance along the X-axis is the path distance from Station No. 123 (the red star in (a)). The three boxes (box1, box2, and box3) in panels (b,c,d) outline the coherent anomalous features in π, AOU and DO, which were identified as subduction patches following the detection procedure in Section 2.2.1. The red lines in panels (b,c,d) indicate the MLD, and the horizontal black lines are the isopycnals. Anomalies of magnitude less than -10 μmol/kg for Δ_{AOU} and ±0.05 kg/m^3 for Δ_{π} (e.g., at section distances of ~25km, 125km, 175km, 275km and 475km) were below our conservative thresholds for identifying intrusions (-10 μmol/kg for Δ_{AOU} and ±0.05 kg/m^3 for Δ_{π}).

Llort et al. (2018) successfully identified eddy subduction in BGC-Argo data from the Southern Ocean using anomalies in spiciness (Flament, 2002; Huang, 2011; McDougall & Krzysik, 2015), a parameter derived from a different function of pressure, temperature, and salinity than potential spicity (Huang et al., 2018). However, we found that spiciness frequently missed signs of subduction while misidentifying other signals as subduction, and the 20-bin method used by Llort et al. (2018) significantly dampened the subduction signals in our data. Potential spicity (π) (Huang et al., 2018), on the other hand, greatly improves the ability to distinguish among similar water masses due to its orthogonal coordination with density; a feature that spiciness lacks. This added sensitivity revealed reliable signals of subduction in these BGC-Argo data. The algorithm based on peak detection here shows better capabilities in capturing and quantifying the subduction signals (see Methods, Fig. S1).

For the same subduction event, continuous subduction patches are expected to be identified from the Argo profiles. The discrete anomalous π and AOU signals, highlighted in boxes 1-3 in the example time series (Fig. 4a, b, c, and d; July 31st, Aug 10th, and August 12th to 15th) indicates that they stemmed from distinct subduction events, opportunistically captured by this BGC-Argo float. The first two anomalies (July and early August) each appeared in only a single profile, perhaps indicating a limited spatial scale of these subduction events. In contrast, the mid-August anomaly persisted over 4 consecutive profiles. We further examined the corresponding time series of temperature, salinity, and potential density, and found salinity also showed similar anomalous signal. As such, we suspect the consecutive subduction patches were most likely from a more sustained, or a larger spatial subduction event. It should be noted that the high detection chance of subduction within 21 days was likely given that the float was trapped in a warm-core eddy (Fig. S2), which does indicate this area is easy to observe subduction events (see Section 3.2).

3.2 Spatial and temporal distributions of subduction

337   We used our peak detection algorithm with the π and AOU data and applied it to all
338   7,120 BGC-Argo profiles (2008-2019) in the western North Pacific (Fig. 5). Our
339   algorithm resolved 335 subduction patches, spread over an unexpectedly large area
340   in the western North Pacific. Overall, subduction patches were identified in 288
341   profiles (4.0%) (some profiles have multiple patches at different depths), with
342   approximately 83% of these being concentrated in the Kuroshio-Oyashio extension
343   region (Fig. 5a). High ($\geq$6 cm) climatologic sea level anomalies (SLA) and the
344   corresponding distribution of Eddy Kinetic Energy (EKE) are evidence of the strong
345   energetic ocean processes in this region (Fig. 5a & 5b). By contrast, far fewer
346   subduction patches were identified in the less energetic region to the south of 29°N
347   despite a higher BGC Argo sampling density (Fig. 2b), consistent with eddy-related
348   processes being important for driving these subduction events. Even so, the true
349   frequency of these events across the entire region is certain to have been under-
350   sampled given their small scales relative to the dispersed BGC-Argo float positions.

EKE (m²/s²)

■ 100~300db (14.6%) ■ 300~450db (33.5%) ■ ≥ 450db (51.9%)

SLA (m)

■ Δ_AOU = -10~-30 μmol/kg (61.7%) ■ Δ_AOU= -30~-50 μmol/kg (20.9%) ■ Δ_AOU ≤ -50 μmol/kg (11.6%)

SLA (m)

■ Spring (38.9%) ■ Summer (31.7%) ■ Fall (21.0%) ■ Winter (8.4%)

351
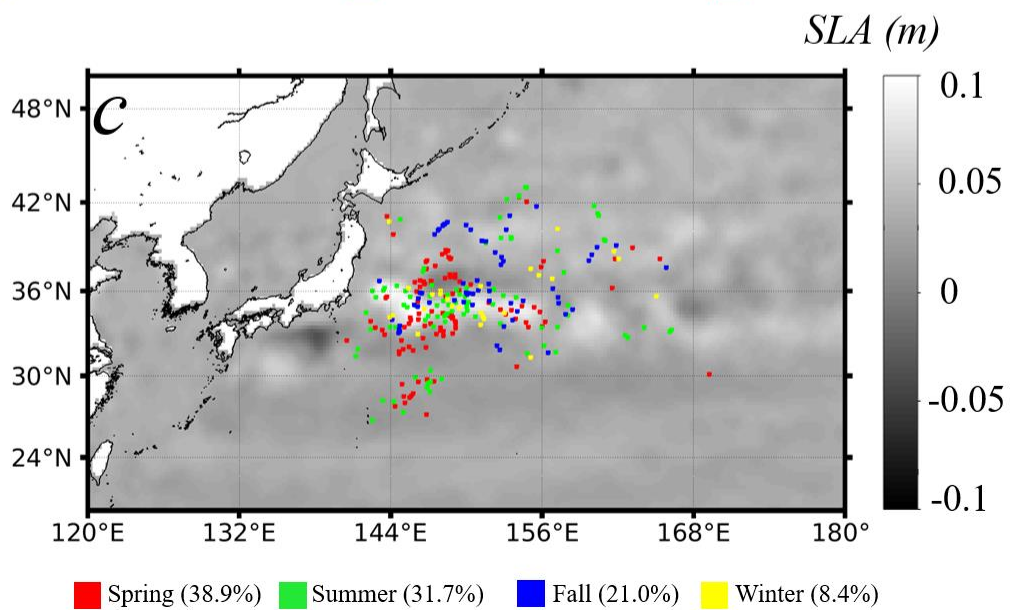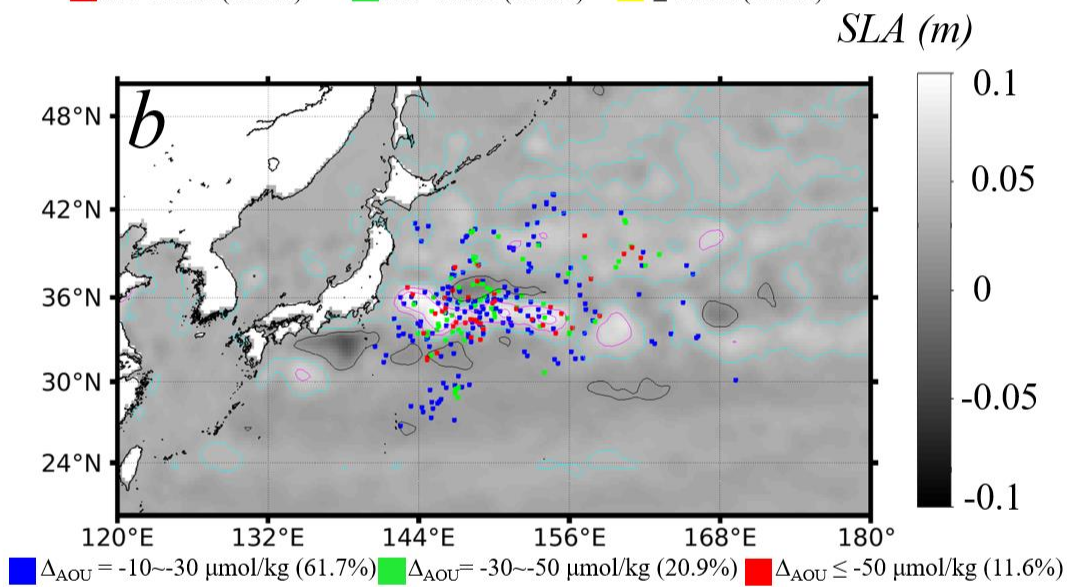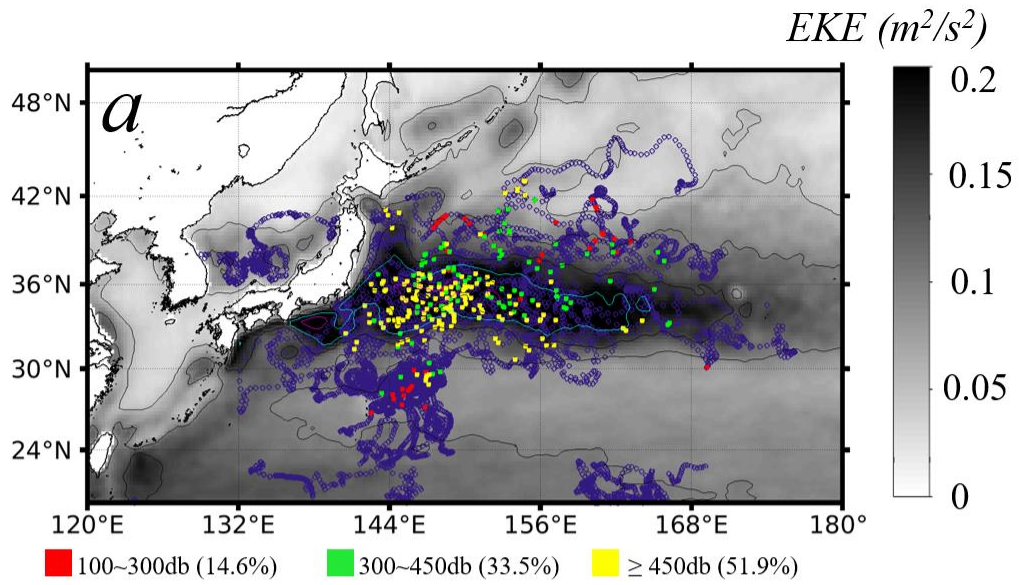
Fig. 5 Horizontal distribution of the BGC-Argo data profiles associated with subduction patches (a and b) between 2008 and 2019 in the western North Pacific. The profiles with detected subduction patches are color coded by different intervals of depths of the subduction patches (a), AOU anomalies (b), and seasons (c), with percentages of detected patches in each interval annotated. The purple background data in (a) represent all the analyzed profiles as shown in Fig. 2a. The grey-scale background map in (a) is the annual mean EKE climatology, with EKE contour lines of 0.3, 0.2, and 0.1 m^2/s^2 shown in magenta, cyan, and black, respectively, and the grey-scale background map in (b) is the annual mean SLA climatology, with SLA contour lines of $\geq$ 0.06, 0.04, and 0.02 m shown in magenta, cyan, and black, respectively. The seasons in (c) is divided with Spring of March-May, Summer of June-Auguest, Fall of September-November, and Winter of December-Febuary.

Discrete signals of subduction were detected throughout the mesopelagic depth range (~100-1000db), with the majority detected below 300db (green and yellow dots in Fig. 5a). The deepest penetrations ($\geq$450 db) occurred largely in areas experiencing the highest EKE while the shallowest (100-300 db) were largely restricted to areas with lower EKE (Fig. 5a). Based on 16 years' Argo float data (N = 1,226,177) in the global ocean, Feucher et al. (2019) found that the depth of permanent pycnocline differs between the subtropical (i.e., < 35 °N) and subpolar (> 35 °N) regions, with the depth of permanent pycnocline to be 300 m and 450 m in the subpolar and subtropical sections of the western North Pacific. Similarly, using the limited BGC-Argo dataset used in this study (Fig. 2), we also found comparably shallower annual maximum MLD in the subpolar section than that in the subtropical section (see Fig. S3). As a result, 56 (16.7%) and 104 (31.0%) subduction patches were found to be above and below the depth the permanent pycnocline (i.e., 450 m) in the subtropical section; and in the subpolar section, 34 (10.1%) and 141 (42.1%) and subduction patches were above and below the permanent pycnocline (i.e., 300 m).Overall, roughly half (52%) of the detected subduction signals were below450 db in this region of the western North Pacific, while 22% penetrated far deeper (up to 800 db; Table S2 in supplemental materials).

There is a distinct seasonality in subduction, with most (~70%) signals being observed between March (the maximum) and August (Figs. 6 & S4), with the peaks appearing in early March. Since these anomalous patches can be observed after their formation, there is a delayed period between the peak of formation and the peak of observation.

Ocean eddies are sustained by many processes including small-scale mixed-layer instabilities set up by large-scale atmospheric forcing in winter (Sasaki1 et al., 2014); in particular, the extreme mixed layer deepening events are attributable to the accumulation of excessive surface cooling driven by synoptic storms in connection with cold-air outbreak (Yu et al., 2020). Each cooling episode brought by the synoptic storm may lead to the formation of subduction patches due to strong mixed layer deepening. Thus, subduction patches are primarily formed during winter and

spring when deep mixing processes occur. Although only 8.3% of the total profiles were obtained in March, they accounted for 17.3% of all observed subduction patches (Fig. S4a), correspondingly, the monthly subduction detection rate (i.e., the number of profiles with identified subduction patches divided by the total number of profiles available) was the highest in March, at ~ 10% (Fig. S5). In a pioneering work, Stommel (1979) argued that a demon working in the ocean by selecting the later winter (typically for later March in the North Hemisphere) water mass properties and injecting them into the subsurface ocean. This mechanism is now called the Stommel Demon in dynamical oceanography (Huang, 2010). The high detection rate of episodic subduction patches in March was consistent with observations of large-scale subduction in this region during late winter, because mesoscale and sub-mesoscale eddy activities are prevalent when large-scale subduction occurs (Qu et al., 2002; Qiu et al., 2007; Nishikawa et al., 2010; Liu & Huang, 2012; Zhang et al., 2014; Xu et al., 2014). The March to August time frame also coincides with the onset and establishment of warming-induced shoaling of the mixed layer depth, when winter-subducted waters are less likely to be re-entrained into surface waters by winds (Dall'Olmo et al., 2016; Palevsky & Doney, 2018). Indeed, based on all the BGC-Argo dataset in Fig. 2, we found that the monthly MLD reached maximum in February and March, and then decreased until August (Fig. S3). It should be noted that, despite the number of subduction patches identified in the time frame of April-August was slightly larger than those in September-December (Fig. S4a), the detection rates did not vary much between these time frames (Fig. S5). In contrast, comparatively few (3.0%) of the subduction patches were detected in January and February, in which time the detection rates were also low (<2%, Fig. S5). Although specific timelines between the observed subduction patches and their formation could not be determined, it is reasonable to anticipate that more energetic winds and the accumulated strong heat loss during mid-winter contributed to the peak in subduction signatures observed in March. However, there were no spatial patterns of the subduction patches detected in each season (Fig. 5c). The current BGC-Argo profiling asset is not sufficient to study

424 how those subduction patches change on interannual scales.

425
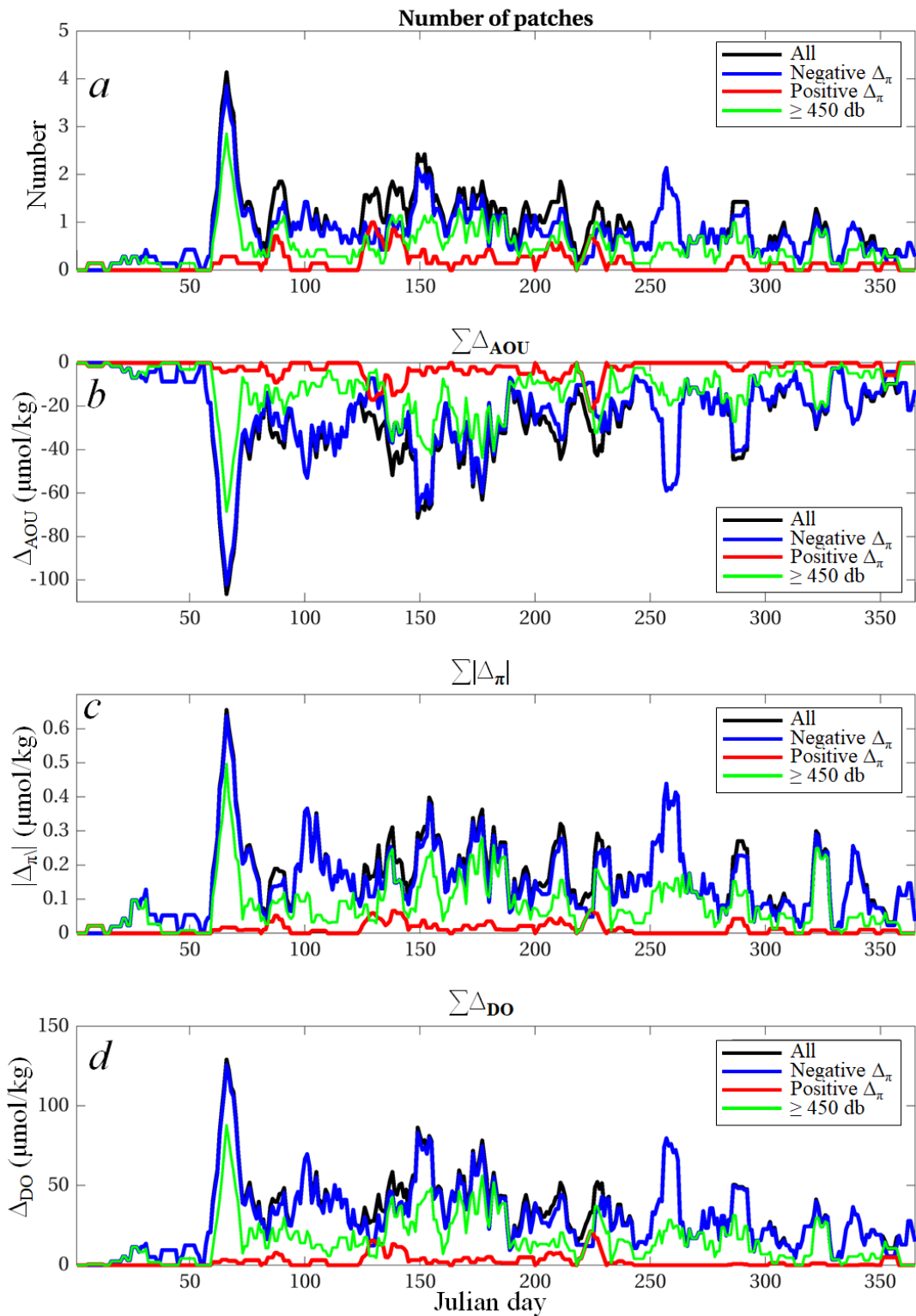
Fig. 6 Temporal distribution of the number of patches (a), integrated AOU anomaly (b), integrated π anomaly (c), and integrated DO anomaly (d), by Julian day based on 7-point smoothing. Spicity in subducted patches can be lower or higher than the surrounding waters, resulting in negative $\Delta\pi$ (red lines) or positive $\Delta\pi$ (blue lines)

anomalies, respectively (see text in Section 3.4). The integrated anomalies indicate the significance and prevalence of the episodic subduction events over time.

The Kuroshio-Oyashio extension zone lies between the subtropical and subpolar gyres in the North Pacific, and it is a recognized hot-spot for water mass exchange via eddy transport (Yasuda et al., 1996; Talley, 1997; Joyce et al., 2001; Zhang et al., 2014; Xu et al., 2016) and substantial ocean-to-atmosphere heat flux (Jing et al., 2020). It is not surprising then that the majority of subduction signals were observed in this region in spite of less float coverage (Fig. 5). In the southern area of the Kuroshio Extension, where the Subtropical Mode Water is formed and the MLD could reach 300-400 m between January and March (Fig. S3). Subduction patches are formed after the water parcels are detached from the base of the mixed layer, and they could be identified below the base of the winter mixing layer (Fig. 5c). Large-scale circulation and seasonal variability in the mixed layer depth here typically result in late winter subduction of subtropical mode waters (Qiu et al., 2007; Oka et al., 2009; Oka & Qiu, 2012; Xu et al., 2014 & 2016), and sharp horizontal density gradients can enhance strong vertical exchanges (Marshall et al., 1993; Hurlburt et al., 1996; Liu et al., 2012; Ma et al., 2017). Rapid heat loss to the winter-time cool, dry continental air masses flowing across the Kuroshio-Oyashio extension erodes the seasonal thermocline to its maximum depth in February-March (Cronin et al., 2013); the latter portion in which the subduction patches were most frequently observed (Fig. 6).

Ascertaining the frequency and spatial extent of these lower-latitude episodic events will be important for establishing their overall contribution to the transport of surface waters into the mesopelagic zone, but this goal is challenged by the presently limited distribution of BGC-Argo floats. It may be possible to obtain a first order estimate of their frequency by linking the subduction signals here to surface-expressed indicators of mesoscale circulation processes. Moreover, our findings suggest that spicity should be adopted more generally in probing BGC-Argo datasets to improve our understanding of the spatial and temporal distribution of subduction processes.

3.3 Properties of subduction patch

Beyond being a water mass indicator, AOU is a proxy for cumulative net community respiration and a sensitive indicator of carbon export in the upper mesopelagic zone (Emerson et al., 2001; Pan et al., 2014; Catala et al., 2018; Bushinsky & Emerson, 2018). This export comprises remineralized carbon as well as dissolved and slowly sinking particulate organic matter carried by the subducting waters (Stukel et al., 2017). The magnitude of AOU may be used as an indicator of the time since subduction, with the first order assumption being that the larger scale processes initiating these subduction events generated similar surface production. Values of Δ_{AOU} at the anomalous peak depth ranged between -10 (the minimal threshold used) and -81 μmol/kg (Fig. 7a). This proxy was highly variable over the space-time domain, similar to the variations in Δ_π (Fig. 7b). In general, 61.7% of the

472 subduction patches had Δ_{AOU} in the range of -30 to -10 μmol/kg with the remainder
473 having greater oxygen depletions (i.e., ≤ -30 μmol/kg) (Figs. 5b). Water masses
474 subducted below 450db (i.e., the permanent pycnocline) had an average AOU
475 anomaly of -25.7±15.3 μmol/kg.
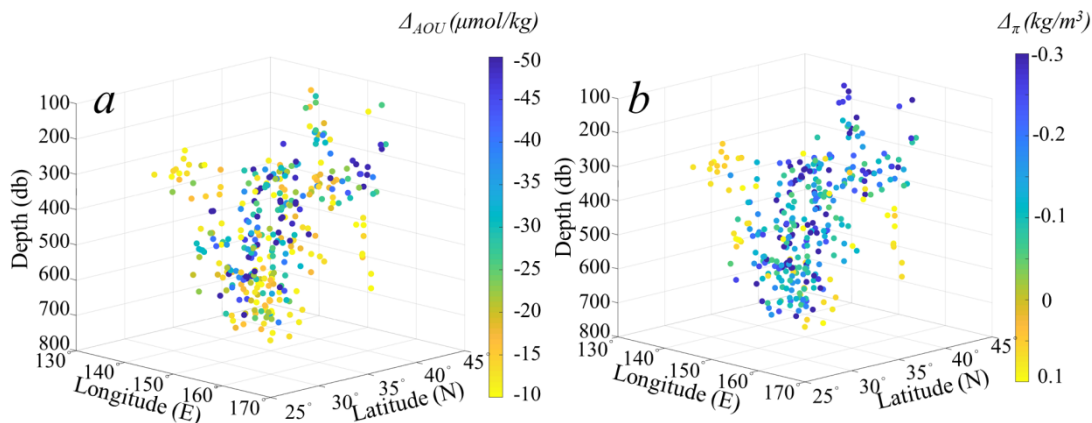
477 **Fig. 7** Vertical spatial distribution of the detected subduction patches in the western
478 North Pacific, color coded by the magnitudes of the subduction strengths in terms of
479 AOU anomaly (a) and π anomaly (b), respectively.

480 There was no clear relationship between the depth of subduction and Δ_{AOU} (Fig 7a),
481 suggesting either surface conditions (e.g., water temperature, primary productivity)
482 were substantially different when the seawater parcels were subducted, or that these
483 signatures stem from non-systematic differences in the time since subducted waters
484 were last at the surface. On the other hand, it is noted in Fig. 7 that the depth
485 positions of the subduction patches appear to somewhat extend from northeast to
486 southwest and deeper along isopycnal surface as illustrated in Fig. 1. This
487 phenomenon is clearly shown when averaging the depth of subduction patches both
488 latitudinally and longitudinally (Fig. S6). Along the latitude, despite a few deep
489 subduction patches identified at 42°-43°N (at around 550m), the mean depths of the
490 subduction patches show a clear increasing pattern from latitude 37°-42°N to
491 latitude of 32°-37°N, i.e., 300m vs. 500m. However, the depth positions tend to be
492 shallower and shallower south of 32°N. Along the longitude, the depth positions
493 generally appear to be deeper from east to west. As such, it is most likely that, the
494 subduction occurred in the northern KE (37°-42°N) could traveled southwestward
495 from shallow to deep depth, and these waters could reach 32°N. The increasing
496 depth positions of subduction patches from 26°N to 32°N tend to suggest the
497 gradually downward movements of the subducted water masses carried by the
498 general trend of the anticyclonic gyre scale circulation, yet a further investigation is
499 needed.

500 In the subpolar region, for the subduction patches identified above and below the
501 depth of permanent pycnocline (i.e., 300 m), respectively, the averaged Δ_{AOU} are -
502 32.9 and -25.8 μmol/kg, averaged Δ_{DO} are 42.5 and 32.5 μmol/kg, averaged
503 thicknesses (i.e., vertical extension of the subduction patch) are 127.5 and 126.6 m

504 (Table 1). In the subtropical region, the depth of permanent pycnocline was deeper
505 (i.e., 450 m), the subduction patches above and below this layer were associated
506 with a mean Δ_{AOU} of -27.2 and -28.5 μmol/kg, mean Δ_{DO} of 31.2 and 36.4 μmol/kg,
507 and mean thickness of 128.7 and 128.1 m (Table 1). In general, the vertical
508 extension (i.e., thickness) of the subduction patches identified in each layer and in
509 each region did not vary much between 126.6 m and 128.7 m. The mean Δ_{AOU} and
510 Δ_{DO} were stronger above the depth of permanent pycnocline than those below the
511 depth of permanent pycnocline in the subpolar region, yet the opposite case shows
512 for the subtropical region, where the mean Δ_{AOU} and Δ_{DO} were weaker above the
513 depth of permanent pycnocline than those below the depth of permanent pycnocline.
514 Interestingly, it is noted that the mean Δ_{AOU} and Δ_{DO} in the subtropical region below
515 450 m were also weaker than those in the subpolar region above 300 m, which
516 further supports the potential northeast-to-southwest pathway of subducted waters
517 shown in Fig. 7.

518 **Table 1** Statistics of the subduction patches and the associated oxygen exports into
519 the ocean's interior. See Section 2.2.2 for details on the calculation of DO inventory.
520 Note that these statistics are based on the subduction patches identified, without
521 considering their episodic characteristics and spatial and temporal inhomogeinity.
522 Note that the DO inventories are the average values of the amount of oxygen into
523 the ocean interior by an episodic subduction event.

Region	Layer	Number of patches	Mean ΔAOU (μmol/kg)	Mean ΔDO (μmol/kg)	Mean thickness (m)	DO inventory$_{IA}$ (g O$_2$ /m^2)	DO inventory$_{PH}$ (g O$_2$ /m^2)
Subtropical	< 450 m	56	-27.2±17.7	31.2±20.4	128.7±27.1	51.7±45.9	132.1±106.2
	≥ 450 m	104	-28.5±15.3	36.4±18.0	128.1±25.8	64.3±50.6	161.5±103.0
Subpolar	< 300 m	34	-32.9±15.5	42.5±17.7	127.5±35.0	92.6±59.7	197.5±115.3
	≥ 300 m	141	-25.8±15.9	32.5±20.9	126.6±23.2	61.2±53.1	142.1±108.1
Whole area	< 450 m	161	-29.7±16.7	36.7±19.7	126.8±26.8	68.5±52.8	160.5±108.0
	≥ 450 m	174	-25.6±15.2	32.5±19.8	128.2±25.1	59.4±52.5	144.3±108.0

524

525 Most subduction patches with strong AOU anomalies were observed between March
526 and August (particularly March, see Fig. S4), after the seasonal mixed layer began to
527 shoal, consistent with expected higher levels of phytoplankton production, which
528 results in a greater degree of respiration in the subducted waters. More respiration
529 means a great degree of oxygen consumption and thus a more negative offset from
530 the surface-saturated concentrations before subduction. Only 0.6% of the total
531 subduction patches had Δ_{AOU} of ≤ -30 μmol/kg in January and February (Fig. S4b).
532 It should be noted that Δ_{AOU} would also strongly depend on the surface water
533 temperature (which determines the solubility of oxygen) when it gets subducted. The
534 π anomalies show similar variation patterns with months (peaked in March), with
535 stronger Δ_π coupled with stronger Δ_{AOU} (Fig. S4c).

536

537 **3.4 Oxygen injections into the twilight zone**

Global ocean inventories of oxygen have been decreasing, and current climate models predict this trend is likely to accelerate over the next century (Oschlies et al., 2018). However, these models suffer from considerable gaps in understanding, one of which is the absence of small-scale transport processes such as the events captured here (Oschlies et al., 2018). The average residual DO enrichment in the subduction patches, defined as the difference in DO concentrations within and adjacent to the subducted waters, was 34.5±19.8 μmol O_2/kg, with levels as high as ~88 μmol O_2/kg below 450 db during March. These differences reflected ~20% higher oxygen concentrations than in the surrounding mesopelagic waters. The integrated DO enrichment reached a maximum in March (Fig. 6d). Based on these residual excess oxygen concentrations, the oxygen inventory within these features was estimated to be on the order of 64 to 152 g O_2 m^{-2} (Eqs. 1 & 2). Specifically, the DO inventories below the permanent pycnocline in the subtropical and subpolar regions were on the order of 64.3-161.5 g O_2 m^{-2} and 61.2-142.1 g O_2 m^{-2}, respectively (Table 1). Note that the DO inventories here are the average values of the amount of oxygen into the ocean interior by an episodic subduction event. These oxygen inventories may represent a significant source of ventilation to our study region.

Co-injection of oxygen below the permanent pycnocline by eddy pumping has not been given close consideration in previous studies, largely because it is less relevant for high latitude, oxygen-rich waters. However, weak ocean ventilation in the tropical and subtropical mesopelagic zone is leading to declining oxygen concentrations (Karstensen et al., 2008; Oschlies et al., 2018; Robinson, 2019) and expansion of oxygen minimum zones in many regions of the oceans (Stramma et al., 2008; Breitburg et al., 2018). These episodic, dispersed subduction events likely represent a significant source of ventilation to help offset the de-oxygenation phenomenon, and to support the expected climate-driven effects of increasing temperature on the metabolic oxygen demand of mesopelagic organisms (Wohlers et al., 2009). Enriched oxygen supplies into the mesopelagic zone also will influence remineralization rates of sinking particulate organic carbon in the ocean's twilight zone (Buesseler et al., 2007; Steinberg et al., 2008) affecting carbon sequestration time scales. Current global-scale biogeochemical models are too coarse to capture the effect that these sub-mesoscale processes may have on mesoscale oxygen variability (Takano et al., 2018), or to account for this additional oxygen supply. Overall, the intensity of these export events below the permanent pycnocline is remarkable, and they should be adequately considered in biogeochemical models.

Eddy associated pumping is also one of several processes contributing to net global ocean carbon export (McGillicuddy, 2016; Boyd et al., 2019), but its importance is generally thought to be comparatively small because the relatively shallow penetration leads to shorter carbon sequestration times (Lévy et al., 2001; Karleskind et al., 2011a & 2011b; Omand et al., 2015; Nagai et al., 2015; Boyd et al., 2019). That is, much of the carbon "exported" to the upper mesopelagic zone over spring and summer is returned to the atmosphere by deep winter mixing. At higher

latitudes, where eddy pumping has been most studied, subduction must extend up to > ~1000 m to reach below the permanent pycnocline (Palevsky & Doney, 2018; Boyd et al., 2019). However, the permanent pycnocline in the western North Pacific is much shallower—on the order of ~300-450 db (Qiu & Huang, 1995; Feucher et al., 2019)—and most of the observed subduction signals here extended far below this depth (Table 1 & S2). Thus although the subduction depths shown here are similar to those observed at higher latitudes, they represent much longer carbon sequestration time scales than those previously associated with eddy pumping (Boyd et al., 2019). As such, in addition to oxygen exports, the observed subduction patches seem to also transport large amounts of carbon into the ocean interior particularly below the permanent pycnocline. However, the lack of carbon measurements on the BGC-Argo floats used in this study impeded us to quantify the carbon inventory within the subduction patches.

Because the BGC-Argo profiler only captures snapshots of subduction events, it is impossible to quantify the vertical transporting rate, which is needed to quantify export fluxes, of subduction from the BGC-Argo float data alone. Alternatively, the lifetime of subduction patches could be used to infer subduction rates, yet due to the dynamics and episodic characteristics of eddy subduction, currently there is no estimates of how much time these water masses maintain differentiated properties in the mesopelagic zone, and there are numerous physical and biogeochemical processes influencing them.

3.5 Surface forcing of subduction

The AOU, DO and π anomalies were integrated within the study domain over the year to assess the extent of subduction in the western North Pacific (Fig. 6, Table 2). π anomalies were divided into negative or positive Δ_π—i.e., π being greater or less than that in surrounding waters—which can suggest their modes of formation. Negative Δ_π would correspond with the subduction of colder and less saline waters, such as along the edges of cyclonic eddies, while positive Δ_π would be associated with the eddy pumping of warmer core, anticyclonic eddies. The subduction patches were clearly dominated by negative Δ_π, and more negative Δ_π corresponded with much larger Δ_{AOU} and Δ_{DO} (Fig. 6, Table 2), suggesting they were associated with cyclonic, cold core, upwelling-dominated eddies that have higher oxygen solubilities, nutrient flux to the surface, and thus higher plankton production. Conversely, the association of lower Δ_{AOU} and Δ_{DO} with positive Δ_π would align with the lower oxygen solubility, nutrient flux and plankton production expected for warmer core, downwelling anticyclonic eddies. Moreover, the majority of deep intrusions had negative Δ_π (Fig. 6, Table 2) consistent with colder waters following deeper isoclines. In contrast, anticyclonic eddies would push warm, lower oxygen and less biomass containing waters to shallower depths. These findings suggest that tracking the activity of cyclonic eddies in regions with shoaling permanent pycnoclines (Chelton et al., 2011; McGillicuddy, 2016) may be particularly important for quantifying these deeper subduction processes.

623 **Table 2** Summary of the subduction patches associated with positive and negative π
624 anomalies; bold numbers indicating statistics of the sum and mean based on absolute
625 values of π anomalies.

Statistics	Number of patches	Δ_{AOU} (μmol/kg)		Δ_{DO} (μmol/kg)		Δ_{π} (kg/m^3)	
		$\sum \Delta_{AOU}$	mean(Δ_{AOU})	$\sum \Delta_{DO}$	mean(Δ_{DO})	$\sum \Delta_{\pi}$	mean(Δ_{π})
Total	335	-9248.43	-27.61	11560.79	34.51	**58.57**	**0.17**
$\Delta_{\pi} < 0$	279	-8303.75	-29.76	10743.84	38.51	-54.16	-0.19
$\Delta_{\pi} > 0$	56	-944.68	-16.87	816.95	14.59	4.41	0.08
Ratio ($\Delta_{\pi} < 0/\Delta_{\pi} > 0$)	4.98	8.79	1.76	13.15	2.64	**12.28**	**2.47**

626 The findings here indicate that eddy associated subduction is an important
627 mechanism driving oxygen enrichment below the permanent pycnocline across the
628 western subtropical Pacific region, particularly near the Kuroshio Extension (KE).
629 Moreover, the abundance of these discrete, small-scale subduction events almost
630 certainly is under-sampled in the BGC-Argo dataset. The frequency of this
631 subduction is expected to vary as the KE oscillates between two dynamic states—
632 quasi-stable and unstable—linked to the Pacific Decadal Oscillation (PDO) or North
633 Pacific Gyre Oscillation (NPGO) (Di Lorenzo et al., 2008). When quasi-stable, the
634 KE jet shifts north and generates less eddy activity than the unstable, highly
635 meandering southward KE jet, which reduces eastward transport and sharply
636 increases eddy kinetic energy (Qiu & Chen, 2010; Lin et al., 2014). Superimposed
637 on these KE oscillations has been an increase in the ratio of cyclonic to anticyclonic
638 eddies associated with a climate-driven intensification of tropical storms in the
639 western Pacific and the multidecadal trend of acceleration in Kuroshio flow (Zhang
640 et al., 2020), suggesting that the importance of eddy-associated subduction processes
641 in this region has been increasing, and may continue to increase in the future. This
642 linkage needs to be considered in designing future ocean observation programs and
643 modeling of global biogeochemical cycles to adequately capture the damping effects
644 that eddy associated subduction may exert on increasing atmospheric CO_2 and de-
645 oxygenation in the tropical and subtropical ocean.

646 4. Conclusion

647 Biogeochemical measurements obtained from the BGC-Argo float data provide new
648 insights into the small-scale vertical water mass exchange in the ocean. In particular,
649 spicity and AOU are key parameters in capturing the episodic subduction events and
650 their significance. Although these floats cannot capture the full pathways of
651 subduction, they provide the first-hand data on locations, depths, time, and strengths
652 of episodic subduction patches. Here we analyze float data in the western North
653 Pacific and show significant subduction export of dissolved oxygen to the
654 mesopelagic zone particularly below the permanent pycnocline; thus, the BGC-Argo
655 data available over the global oceans can be used to extend the current study to other
656 oceanic regions. Carbon measurements are needed to quantify the carbon export
657 associated with the subduction patches. These two factors—carbon export and re-

658 oxygenation—would help to offset the apparent budget imbalance between the
659 biological gravitational pump and mesopelagic carbon demand, and support the
660 increasing metabolic oxygen demand of mesopelagic organisms as ocean warming
661 continues.

Acknowledgements

663 This work was supported the National Natural Science Foundation of China (NSFC)
664 projects (41906159, 42030708, and 41730536), the Scientific Research Fund of the
665 Second Institute of Oceanography, MNR (14283), and the Marine S&T Fund of
666 Shandong Province for Pilot National Laboratory for Marine Science and
667 Technology (Qingdao) (2018SDKJ0206). The authors thank Dr. Joan Llort and two
668 other anonymous reviewers helping us improve the manuscript.

Author contributions

670 S. C. was responsible for data processing and drafting the manuscript, R. X. H. and
671 H. X. took the lead in data analysis from the view of physical oceanography, M. L.
672 W. and F. C. contributed to the biogeochemical analysis, and F. C. designed and
673 coordinated the overall research project. All authors contributed to the ideas and
674 writing of this manuscript.

Competing interests

676 The authors declare no competing financial or research interests.

Data availability

678 The BGC-Argo data used in this study were collected and made freely available by
679 the International Argo Program and the national programs that contribute to it
680 (http://www.argo.ucsd.edu, http://argo.jcommops.org), archived in the Argo Global
681 Data Assembly Centre (http://doi.org/10.17882/42182), and quality-controlled and
682 made available by the China Argo Real-time Data Center (http://www.argo.org.cn).
683 The satellite SLA and geostrophic velocity data are from the Archiving, Validation
684 and Interpretation of Satellite Data in Oceanography (AVISO) and can be
685 downloaded from the Copernicus Marine Environment Monitoring Service
686 (https://marine.copernicus.eu/).

References

688 Boyd, P.W., Claustre, H., Levy, M., Siegel, D.A. and Weber, T., 2019. Multi-
689 faceted particle pumps drive carbon sequestration in the ocean. Nature,
690 568(7752), 327-335.
691 Brainerd, K. E., & Gregg, M. C., 1995. Surface mixed and mixing layer depths.
692 Deep Sea Research Part I: Oceanographic Research Papers, 42(9), 1521-1543.
693 Breitburg, D., Levin, L. A., Oschlies, A., Grégoire, M., Chavez, F. P., Conley, D.
694 J., ... & Jacinto, G. S., 2018. Declining oxygen in the global ocean and coastal
695 waters. Science, 359(6371), eaam7240.

696 Buesseler, K. O., Lamborg, C. H., Boyd, P. W., Lam, P. J., Trull, T. W., Bidigare, R.
697   R., ... & Honda, M., 2007. Revisiting Carbon Flux Through the Ocean's Twilight
698   Zone. Science, 316(5824), 567-570.
699 Bushinsky, S. M., & Emerson, S. R., 2018. Biological and physical controls on the
700   oxygen cycle in the Kuroshio Extension from an array of profiling floats. Deep
701   Sea Research Part I: Oceanographic Research Papers, 141, 51-70.
702 Catala, T. S., Martinez-Perez, A. M., Nieto-Cid, M., Alvarez, M., Otero, J.,
703   Emelianov, M., Reche, I., Aristegui, J., & Alvarez-Salgado, X. A., 2018.
704   Dissolved Organic Matter (DOM) in the open Mediterranean Sea. I. Basin-wide
705   distribution and drivers of chromophoric DOM. Progress in Oceanography, 165,
706   35-51. doi:10.1016/j.pocean.2018.05.002
707 Chai, F., Johnson, K. S., Claustre, H., Xing, X., Wang, Y., Boss, E., ... & Sutton, A.,
708   2020. Monitoring ocean biogeochemistry with autonomous platforms. Nature
709   Reviews Earth & Environment, 1, 315-326.
710 Chelton, D. B., Schlax, M. G., & Samelson, R. M., 2011. Global observations of
711   nonlinear mesoscale eddies. Progress in oceanography, 91(2), 167-216.
712 Claustre, H., Johnson, K.S. and Takeshita, Y., 2020. Observing the Global Ocean
713   with Biogeochemical-Argo. Annual review of marine science, 12, 11.1-11.26.
714 Cronin, M. F., Bond, N. A., Farrar, J. T., Ichikawa, H., Jayne, S. R., Kawai, Y.,
715   Konda, M., Qiu, B., Rainville, L., & Tomita, H., 2013. Formation and erosion of
716   the seasonal thermocline in the Kuroshio Extension Recirculation Gyre. Deep-
717   Sea Research Part II-Topical Studies in Oceanography, 85, 62-74.
718   doi:10.1016/j.dsr2.2012.07.018
719 Dall'Olmo, G., Dingle, J., Polimene, L., Brewin, R.J. and Claustre, H., 2016.
720   Substantial energy input to the mesopelagic ecosystem from the seasonal mixed-
721   layer pump. Nature Geoscience, 9(11), 820-823.
722 Di Lorenzo, E., Schneider, N., Cobb, K. M., Franks, P. J. S., Chhak, K., Miller, A.
723   J., ... & Powell, T. M., 2008. North Pacific Gyre Oscillation links ocean climate
724   and ecosystem change. Geophysical Research Letters, 35(8).
725 Emerson, S., Mecking, S., & Abell, J., 2001. The biological pump in the subtropical
726   North Pacific Ocean: Nutrient sources, Redfield ratios, and recent changes.
727   Global biogeochemical cycles, 15(3), 535-554.
728 Emerson, S., 2014. Annual net community production and the biological carbon flux
729   in the ocean. Global Biogeochemical Cycles, 28(1), 14-28.
730 Estapa, M. L., Feen, M. L., & Breves, E., 2019. Direct observations of biological
731   carbon export from profiling floats in the subtropical North Atlantic. Global
732   Biogeochemical Cycles, 33(3), 282-300.
733 Feucher, C., Maze, G., & Mercier, H., 2019. Subtropical mode water and permanent
734   pycnocline properties in the world ocean. Journal of Geophysical Research:
735   Oceans, 124(2), 1139-1154.
736 Flament, P., 2002. A state variable for characterizing water masses and their
737   diffusive stability: spiciness. Progress in Oceanography, 54(1-4), 493-501.
738 Garcia, H.E. and Gordon, L.I., 1992. Oxygen solubility in seawater: Better fitting
739   equations. Limnology and oceanography, 37(6), 1307-1312.

740 Hosoda, S., Inoue, R., Nonaka, M., Sasaki, H., Sasai, Y., & Hirano, M., 2021. Rapid
741   water parcel transport across the Kuroshio Extension in the lower thermocline
742   from dissolved oxygen measurements by Seaglider. Progress in Earth and
743   Planetary Science, 8(1), 1-19.

744 Huang, R. X., 2010. Ocean Circulation, wind-driven and thermohaline processes,
745   Cambridge Press, 810pp.

746 Huang, R. X., 2011. Defining the spicity. Journal of Marine Research, 69(4-5), 545-
747   559.

748 Huang, R.X., Yu, L.-S. and Zhou, S.-Q., 2018. Potential spicity defined by the least
749   square method, Journal of Geophysical Research, Ocean, 123, 7351-7365.

750 Hurlburt, H.E., Wallcraft, A.J., Schmitz Jr, W.J., Hogan, P.J. and Metzger, E.J.,
751   1996. Dynamics of the Kuroshio/Oyashio current system using eddy-resolving
752   models of the North Pacific Ocean. Journal of Geophysical Research: Oceans,
753   101(C1), 941-976.

754 Inoue, R., Honda, M. C., Fujiki, T., Matsumoto, K., Kouketsu, S., Suga, T., & Saino,
755   T., 2016a. Western North Pacific integrated physical-biogeochemical ocean
756   observation experiment (INBOX): Part 2. Biogeochemical responses to eddies
757   and typhoons revealed from the S1 mooring and shipboard measurements.
758   Journal of Marine Research, 74(2), 71-99.

759 Inoue, R., Suga, T., Kouketsu, S., Kita, T., Hosoda, S., Kobayashi, T., ... & Kawano,
760   T., 2016b. Western north Pacific integrated physical-biogeochemical ocean
761   observation experiment (INBOX): part 1. Specifications and chronology of the
762   S1-INBOX floats. Journal of Marine Research, 74(2), 43-69.

763 Jing, Z., Wang, S., Wu, L., Chang, P., Zhang, Q., Sun, B., ... & Chen, Z., 2020.
764   Maintenance of mid-latitude oceanic fronts by mesoscale eddies. Science
765   advances, 6(31), eaba7880.

766 Joyce, T. M., Yasuda, I., Hiroe, Y., Komatsu, K., Kawasaki, K., & Bahr, F., 2001.
767   Mixing in the meandering Kuroshio Extension and the formation of North
768   Pacific Intermediate Water. Journal of Geophysical Research: Oceans, 106(C3),
769   4397-4404.

770 Karleskind, P., Lévy, M., & Mémery, L., 2011a. Subduction of carbon, nitrogen, and
771   oxygen in the northeast Atlantic. Journal of Geophysical Research: Oceans,
772   116(C2).

773 Karleskind, P., Lévy, M., & Mémery, L., 2011b. Modifications of mode water
774   properties by sub-mesoscales in a bio-physical model of the Northeast Atlantic.
775   Ocean Modelling, 39(1-2), 47-60.

776 Karstensen, J., Stramma, L., & Visbeck, M., 2008. Oxygen minimum zones in the
777   eastern tropical Atlantic and Pacific oceans. Progress in Oceanography, 77(4),
778   331-350.

779 Kawakami, Y., Sugimoto, S., and Suga, T., 2015. Inter-annual zonal shift of the
780   formation region of the lighter variety of the north pacific central mode water.
781   Journal of Oceanography, 72(2), 1-10.

782   Koch-Larrouy, A., Morrow, R., Penduff, T. and Juza, M., 2010. Origin and
783   mechanism of Subantarctic Mode Water formation and transformation in the
784   Southern Indian Ocean. Ocean Dynamics, 60(3), 563-583.

785   Kouketsu, S., Inoue, R., & Suga, T., 2016. Western North Pacific integrated
786   physical-biogeochemical ocean observation experiment (INBOX): part 3.
787   Mesoscale variability of dissolved oxygen concentrations observed by multiple
788   floats during S1-INBOX. Journal of Marine Research, 74(2), 101-131.

789   Lévy, M., Klein, P. and Treguier, A.M., 2001. Impact of sub-mesoscale physics on
790   production and subduction of phytoplankton in an oligotrophic regime. Journal
791   of Marine Research, 59(4), 535-565.

792   Lin, P., Chai, F., Xue, H., & Xiu, P., 2014. Modulation of decadal oscillation on
793   surface chlorophyll in the Kuroshio Extension. Journal of Geophysical Research:
794   Oceans, 119(1), 187-199.

795   Liu, L. L. and Huang, R.X., 2012. The global subduction/obduction rates: Their
796   interannual and decadal variability. Journal of Climate, 25(4), 1096-1115.

797   Liu, Y., Dong, C., Guan, Y., Chen, D., McWilliams, J. and Nencioli, F., 2012. Eddy
798   analysis in the subtropical zonal band of the North Pacific Ocean. Deep Sea
799   Research Part I: Oceanographic Research Papers, 68, 54-67.

800   Llort, J., Langlais, C., Matear, R., Moreau, S., Lenton, A. and Strutton, P.G., 2018.
801   Evaluating Southern Ocean carbon eddy-pump from biogeochemical-Argo floats.
802   Journal of Geophysical Research: Oceans, 123(2), 971-984.

803   Ma, X., Chang, P., Saravanan, R., Montuoro, R., Nakamura, H., Wu, D., Lin, X. and
804   Wu, L., 2017. Importance of resolving Kuroshio front and eddy influence in
805   simulating the North Pacific storm track. Journal of Climate, 30(5), 1861-1880.

806   Marshall, J.C., Williams, R.G. and Nurser, A.G., 1993. Inferring the subduction rate
807   and period over the North Atlantic. Journal of Physical Oceanography, 23(7),
808   1315-1329.

809   Martin, A., Boyd, P., Buesseler, K., Cetinic, I., Claustre, H., Giering, S., ... &
810   Robinson, C., 2020. The oceans' twilight zone must be studied now, before it is
811   too late. Nature, 580, 26-28.

812   McDougall, T., & Barker, P., 2011. Getting started with TEOS-10 and the Gibbs
813   Seawater (GSW) oceanographic toolbox. SCOR/IAPSO, WG127, pp 28.

814   McDougall, T. J., & Krzysik, O. A., 2015. Spiciness. Journal of Marine Research,
815   73(5), 141-152.

816   McGillicuddy, D.J., 2016. Mechanisms of Physical-Biological-Biogeochemical
817   Interaction at the Oceanic Mesoscale. Annual Review of Marine Science, 8, 125-
818   159.

819   Nagai, T., Gruber, N., Frenzel, H., Lachkar, Z., McWilliams, J. C., & Plattner, G. K.,
820   2015. Dominant role of eddies and filaments in the offshore transport of carbon
821   and nutrients in the California Current System. Journal of Geophysical Research:
822   Oceans, 120(8), 5318-5341.

823   Nagano, A., Suga, T., Kawai, Y., Wakita, M., Uehara, K., & Taniguchi, K., 2016.
824   Ventilation revealed by the observation of dissolved oxygen concentration south

of the Kuroshio Extension during 2012–2013. Journal of Oceanography, 72(6), 837-850.

Nie, X., Gao, S., Wang, F., & Qu, T., 2016. Subduction of north pacific tropical water and its equatorward pathways as shown by a simulated passive tracer. Journal of Geophysical Research: Oceans, 121.

Nishikawa, S., Tsujino, H., Sakamoto, K. and Nakano, H., 2010. Effects of mesoscale eddies on subduction and distribution of subtropical mode water in an eddy-resolving OGCM of the western North Pacific. Journal of Physical Oceanography, 40(8), 1748-1765.

Oka, E., Toyama, K. and Suga, T., 2009. Subduction of North Pacific central mode water associated with subsurface mesoscale eddy. Geophysical Research Letters, 36(8), L08607.

Oka, E. and Qiu, B., 2012. Progress of North Pacific mode water research in the past decade. Journal of oceanography, 68(1), 5-20.

Okuda, K., Yasuda, I., Hiroe, Y., & Shimizu, Y., 2001. Structure of subsurface intrusion of the Oyashio water into the Kuroshio Extension and formation process of the North Pacific Intermediate Water. Journal of oceanography, 57(2), 121-140.

Omand, M.M., D'Asaro, E.A., Lee, C.M., Perry, M.J., Briggs, N., Cetinić, I. and Mahadevan, A., 2015. Eddy-driven subduction exports particulate organic carbon from the spring bloom. Science, 348(6231), 222-225.

Oschlies, A., Brandt, P., Stramma, L., & Schmidtko, S., 2018. Drivers and mechanisms of ocean deoxygenation. Nature Geoscience, 11(7), 467-473.

Palevsky, H. I., & Doney, S. C., 2018. How choice of depth horizon influences the estimated spatial patterns and global magnitude of ocean carbon export flux. Geophysical Research Letters, 45, 4171–4179. https://doi.org/10.1029/2017GL076498

Pan, X., Achterberg, E. P., Sanders, R., Poulton, A. J., Oliver, K. I., & Robinson, C., 2014. Dissolved organic carbon and apparent oxygen utilization in the Atlantic Ocean. Deep Sea Research Part I: Oceanographic Research Papers, 85, 80-87.

Qiu, B., & Huang, R. X., 1995. Ventilation of the North Atlantic and North Pacific: subduction versus obduction. Journal of Physical Oceanography, 25(10), 2374-2390.

Qiu, B., Chen, S. and Hacker, P., 2007. Effect of mesoscale eddies on subtropical mode water variability from the Kuroshio Extension System Study (KESS). Journal of Physical Oceanography, 37(4), 982-1000.

Qiu, B., & Chen, S., 2010. Eddy-mean flow interaction in the decadally modulating Kuroshio Extension system. Deep Sea Research Part II: Topical Studies in Oceanography, 57(13-14), 1098-1110.

Qu, T., Xie, S.P., Mitsudera, H. and Ishida, A., 2002. Subduction of the North Pacific mode waters in a global high-resolution GCM. Journal of physical oceanography, 32(3), 746-763.

Qu, T. and Chen, J., 2009. A North Pacific decadal variability in subduction rate. Geophysical Research Letters, 36(22), L22602.

869   Resplandy, L., Lévy, M. and Mcgillicuddy, D.J., 2019. Effects of eddy−driven
870   subduction on ocean biological carbon pump. Global Biogeochemical Cycles,
871   33(8), pp.1071-1084.

872   Robinson, C., 2019. Microbial respiration, the engine of ocean deoxygenation.
873   Frontiers in Marine Science, 5, 533.

874   Sabine, C.L., Feely, R.A., Gruber, N., Key, R.M., Lee, K., Bullister, J.L.,
875   Wanninkhof, R., Wong, C.S.L., Wallace, D.W., Tilbrook, B. and Millero, F.J.,
876   2004. The oceanic sink for anthropogenic CO_2. Science, 305(5682), 367-371.

877   Sarmiento, J.L., & Gruber, N., 2006. Ocean biogeochemical dynamics. Princeton
878   University Press.

879   Stommel, H. M., 1979. Determination of water mass properties of water pumped
880   down from the Ekman layer to the geostrophic flow below. Proc. Natl. Acad. Sci.
881   U.S.A., 76, 3051-3055.

882   Steinberg, D. K., Van Mooy, B. A., Buesseler, K. O., Boyd, P. W., Kobari, T., &
883   Karl, D. M., 2008. Bacterial vs. zooplankton control of sinking particle flux in
884   the ocean's twilight zone. Limnology and Oceanography, 53(4), 1327-1338.

885   Stramma, L., Johnson, G. C., Sprintall, J., & Mohrholz, V., 2008. Expanding
886   oxygen-minimum zones in the tropical oceans. science, 320(5876), 655-658.

887   Stukel, M.R., Aluwihare, L.I., Barbeau, K.A., Chekalyuk, A.M., Goericke, R.,
888   Miller, A.J., Ohman, M.D., Ruacho, A., Song, H., Stephens, B.M. and Landry,
889   M.R., 2017. Mesoscale ocean fronts enhance carbon export due to gravitational
890   sinking and subduction. Proceedings of the National Academy of Sciences of the
891   United States of America, 114(6), 1252-1257.

892   Stukel, M.R., Song, H., Goericke, R. and Miller, A.J., 2018. The role of subduction
893   and gravitational sinking in particle export, carbon sequestration, and the
894   remineralization length scale in the California Current Ecosystem. Limnology
895   and Oceanography, 63(1), 363-383.

896   Takano, Y., Ito, T., & Deutsch, C., 2018. Projected centennial oxygen trends and
897   their attribution to distinct ocean climate forcings. Global Biogeochemical
898   Cycles, 32(9), 1329-1349.

899   Talley, L. D., 1997. North Pacific Intermediate Water transports in the mixed water
900   region. Journal of physical oceanography, 27(8), 1795-1803.

901   Williams, R.G., 2001. Ocean Subduction, in: Encyclopedia of Ocean Sciences.
902   Elsevier, pp. 1982–1993.

903   Wohlers, J., Engel, A., Zöllner, E., Breithaupt, P., Jürgens, K., Hoppe, H. G., ... &
904   Riebesell, U., 2009. Changes in biogenic carbon flow in response to sea surface
905   warming. Proceedings of the national academy of sciences, 106(17), 7067-7072.

906   Sasaki, H., Klein, P., Qiu, B. et al., 2014. Impact of oceanic-scale interactions on the
907   seasonal modulation of ocean dynamics by the atmosphere. Nature
908   Communication 5, 5636. https://doi.org/10.1038/ncomms6636

909   Xu, L., Xie, S.P., McClean, J.L., Liu, Q. and Sasaki, H., 2014. Mesoscale eddy
910   effects on the subduction of North Pacific mode waters. Journal of Geophysical
911   Research: Oceans, 119(8), 4867-4886.

912   Xu, L., Li, P., Xie, S.P., Liu, Q., Liu, C. and Gao, W., 2016. Observing mesoscale
913   eddy effects on mode-water subduction and transport in the North Pacific.
914   Nature communications, 7, 10505.
915   Yasuda, I., Okuda, K., & Shimizu, Y., 1996. Distribution and modification of North
916   Pacific Intermediate Water in the Kuroshio-Oyashio interfrontal zone. Journal of
917   physical oceanography, 26(4), 448-465.
918   Yu, J., Gan, B., Zhao J., & Wu, L., 2020, Winter Extreme Mixed Layer Depth South
919   of the Kuroshio Extension, J. Climate, DOI: 10.1175/JCLI-D-20-0119.1
920   Zhang, Z., Wang, W., & Qiu, B., 2014. Oceanic mass transport by mesoscale eddies.
921   Science, 345(6194), 322-324.
922   Zhang, Z., Li, P., Xu, L., Li, C., Zhao, W., Tian, J., & Qu, T., 2015. Subthermocline
923   eddies observed by rapid-sampling Argo floats in the subtropical northwestern
924   Pacific Ocean in Spring 2014. Geophysical Research Letters, 42(15), 6438-6445.
925   Zhang, Y., Zhang, Z., Chen, D., Qiu, B., & Wang, W., 2020. Strengthening of the
926   Kuroshio current by intensifying tropical cyclones. Science, 368(6494), 988-993.
927   Zhu, R., Chen, Z., Zhang, Z., Yang, H., & Wu, L., 2021. Subthermocline eddies in
928   the Kuroshio Extension region observed by mooring arrays. Journal of Physical
929   Oceanography, 51(2), 439-455.